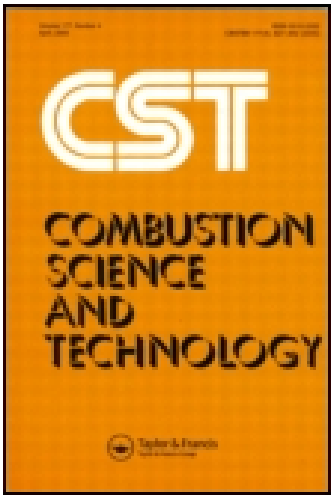

Combustion Science and Technology
Publication details, including instructions for authors and subscription information:
http://www.tandfonline.com/loi/gcst20

Counterflow Diffusion Flames of Oxygen and N-Alkane Hydrocarbons (CH_4-$C_{16}H_{34}$) at Subcritical and Supercritical Conditions

Xingjian Wang[a], Hongfa Huo[a] & Vigor Yang[a]
[a] School of Aerospace Engineering, Georgia Institute of Technology, Atlanta, Georgia, USA
Published online: 10 Dec 2015.

To cite this article: Xingjian Wang, Hongfa Huo & Vigor Yang (2015) Counterflow Diffusion Flames of Oxygen and N-Alkane Hydrocarbons (CH_4-$C_{16}H_{34}$) at Subcritical and Supercritical Conditions, Combustion Science and Technology, 187:1-2, 60-82, DOI: 10.1080/00102202.2014.973955

To link to this article: http://dx.doi.org/10.1080/00102202.2014.973955

Combust. Sci. Technol., 187: 60–82, 2015

ISSN: 0010-2202 print / 1563-521X online
DOI: 10.1080/00102202.2014.973955

Taylor & Francis
Taylor & Francis Group

COUNTERFLOW DIFFUSION FLAMES OF OXYGEN AND N-ALKANE HYDROCARBONS (CH_4-$C_{16}H_{34}$) AT SUBCRITICAL AND SUPERCRITICAL CONDITIONS

Xingjian Wang, Hongfa Huo, and Vigor Yang

School of Aerospace Engineering, Georgia Institute of Technology, Atlanta, Georgia, USA

This article presents an investigation of counterflow diffusion flames of oxygen and n-alkanes (CH_4-$C_{16}H_{34}$) over the entire thermodynamic fluid regime and a wide range of flow strain rates. The formulation incorporates fundamental thermodynamics and transport theories, along with detailed chemistry. An improved two-point flame-controlling continuation method is employed to capture the complete flame response along the S-curve. Two selected members of the n-alkane family, methane and n-heptane, are studied in detail. The results confirm that the flame thickness (δ) and the global heat-release rate ($\dot{q}$) of oxygen/hydrocarbon systems are closely related to the pressure-weighted strain rate, $\delta \sim 1/\sqrt{pa}$ and $\dot{q} \sim \sqrt{pa}$. The latter correlation is further modified to account for the pressure effect on peak flame temperature, $\dot{q} \sim p^{0.536}\sqrt{a}$ for the oxygen/methane system, $\dot{q} \sim p^{0.534}\sqrt{a}$ for the oxygen/n-heptane system. The inlet temperature appears to have a negligible effect on flame characteristics. General similarities are developed in the mixture-fraction space in terms of flame temperature, species concentrations, flame thickness, and heat-release rate for all pressures under consideration. This suggests that the flame behaviors at high pressure can be evaluated by their counterpart at low pressure. The common features for the n-alkane family are identified. The flame properties of a given hydrocarbon fuel can be predicted from those of another hydrocarbon fuel at the same flow conditions. The results contribute to the establishment of a tabulated chemistry library for the modeling of supercritical combustion of oxygen and hydrocarbon fuels.

Keywords: *n*-Alkane; Counterflow diffusion flame; Flame similarity; High-pressure combustion; Strain rate

INTRODUCTION

Counterflow diffusion flames have been extensively studied by means of analytical, experimental, and numerical techniques, and flame behaviors and burning properties have been characterized for a wide variety of fuel and oxidizer combinations under a broad range of flow conditions (Law, 2006; Williams, 1985). Until recently, however, most of the studies were carried out at room conditions, based on an ideal-gas assumption. The

Received 28 September 2014; revised 2 October 2014; accepted 3 October 2014.

Published as part of the Special Issue in Honor of Professor Forman A. Williams on the Occasion of His 80th Birthday with Guest Editors Chung K. Law and Vigor Yang.

Address correspondence to Vigor Yang, Daniel Guggenheim School of Aerospace Engineering, Georgia Institute of Technology, 313 Montgomery Knight Building, Atlanta, GA 30332-0150, USA. E-mail: vigor.yang@aerospace.gatech.edu

Color versions of one or more of the figures in the article can be found online at www.tandfonline.com/gcst.

flame structures and dynamics at high pressure, which occur in many practical combustion devices, have been less thoroughly explored.

Ribert et al. (2008) conducted a pioneering analysis of counterflow diffusion flames for real fluids. The model employs a unified treatment of fundamental thermodynamics and transport theories (Yang, 2000) and is thus capable of handling flow and flame evolution over the entire regime of thermodynamic fluid states. As a specific example, the oxygen/hydrogen system was treated in depth. The effects of the cryogenic fluid properties of oxygen on the flame characteristics were explored. It was found that the flame thickness and heat-release rate correlate well with the square root of the product of pressure and strain rate, $\sqrt{pa}$. Following an approach similar to Ribert et al. (2008), Lacaze and Oefelein (2012) developed a flamelet model that combines real-fluid thermodynamics with a tabulated chemistry to study combustion instabilities in practical burners. These studies only considered stable burning with moderate flow-strain rates. The flame behaviors near the extinction point were not investigated. Huo et al. (2014) established a general framework for the first time for real fluids to investigate the flame responses over the entire S-curve by implementing an improved two-point flame-controlling method. General similarities of flame temperature, flame thickness, species concentration, and heat-release rate were found in a normalized strain-rate space for the range of pressures under consideration. This finding can be effectively used to improve the computational efficiency of combustion modeling using tabulated chemistry.

Existing studies of high-pressure counterflow diffusion flames mainly focus on the oxygen/hydrogen system. Limited attention has been given to hydrocarbon fuels, which are used for a vast majority of combustion devices, including gas-turbine, liquid-rocket, and diesel engines. Pons et al. (2008) studied the pressure effects of oxygen/methane flames. A fast-chemistry assumption was applied to derive scaling factors for characterizing flame properties. The analysis employed ideal-gas thermophysical properties with supercritical inlet temperatures. Pons et al. (2009) later studied mass transfer and combustion in transcritical non-premixed oxygen/methane counterflows. Real-fluid properties were employed by extending the standard Chemkin package to the transcritical regime. The flame was established in the light-gas region adjacent to the sharp density gradient in the transcritical zone. The work only considered the effect of inlet temperature on the flame structure at a pressure of 7 MPa under stable burning conditions. A more complete investigation of the flame behaviors, including extinction characteristics, is needed for a broad range of pressures and strain rates.

Heavy hydrocarbon combustion with air in a counterflow setting has been the subject of many studies. Li and Williams (2000) performed both experimental and numerical investigations of diffusion and partially-premixed air/*n*-heptane flames. It was concluded that a reduced mechanism of 36 species and 180 reactions is insufficient for accurate prediction of intermediate species. Seiser et al. (2000) explored the extinction and auto-ignition of *n*-heptane counterflow flames at atmospheric conditions. The effect of strain rate was found to be more influential on the low-temperature chemistry than on the reactant temperature. Efforts were also made to develop more detailed chemical mechanisms for *n*-heptane oxidation. Curran et al. (1998) developed a comprehensive mechanism consisting of 556 species and 2540 reversible reaction steps, which was verified for pressures up to 42 atm. This mechanism was further modified and extended for C_8-C_{16} normal alkanes (Westbrook et al., 2009), and will be used in the present work. Most of the previous studies operated at either low pressures or low strain rates for diluted fuel and air. Furthermore, reduced chemical

mechanisms were often employed. A systematic investigation into the flame properties under a wide range of flow conditions is yet to be performed.

The purpose of the present study is to explore the characteristics of counterflow diffusion flames of oxygen and hydrocarbon fuels. A wide range of *n*-alkanes (CH_4-$C_{16}H_{34}$) will be treated under both subcritical and supercritical conditions. The behaviors of oxygen/hydrogen flames will also be noted as a benchmark. The work extends the general framework of Huo et al. (2014) and accommodates detailed chemical kinetics and fluid properties of hydrocarbon fuels. Emphasis will be given to the effects of pressure, inlet temperature, and strain rate on the flame structures and burning behaviors, including extinction, heat-release rate, and flame temperature, as well as the temperature and species distributions. The flame response over the entire S-curve will be obtained, and general correlations will be developed systematically.

The article is organized as follows. The following section describes the theoretical formulation based on general-fluid thermodynamics and transport theories. In the Results and Discussion section, the behaviors of oxygen/methane and oxygen/*n*-heptane flames are studied in detail and the common features for the *n*-alkane family (CH_4-$C_{16}H_{34}$) are then summarized.

THEORETICAL FORMULATION

The physical model of concern is a counterflow diffusion flame generated by two opposing fluid jets issuing from two circular nozzles, as shown in Figure 1. This axisymmetric geometry significantly simplifies the governing equations to a quasi one-dimensional (1D) framework (Kee et al., 1989). The theoretical framework was introduced in detail by Huo et al. (2014), and applied to study the oxygen/hydrogen system over a wide range of thermodynamic fluid states and flow conditions. The formulation accommodates the conservation equations of mass, momentum, species, and energy, and takes full account of general-fluid thermodynamics and transport phenomena. Thermodynamic properties, including enthalpy, specific heats, and internal energy, are derived from fundamental thermodynamic theories. They are expressed as the sum of an ideal-gas property at the given temperature and a departure function accounting for dense-fluid corrections (Yang, 2000). The latter requires a robust equation of state that correlates density and temperature with pressure. A modified Soave–Redlich–Kong (SRK) equation of state (Soave, 1972) is employed because of its easy implementation and validity over a broad range of fluid states.

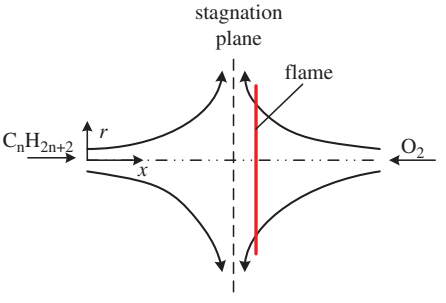

Figure 1 Schematic diagram of a counterflow diffusion flame.

Transport properties are determined by means of the corresponding state principles. Details of the overall property evaluation scheme can be found in Yang (2000).

The integrated theoretical model and numerical method is capable of treating the flame responses for general fluids over the entire S-curve, including both the stable and unstable branches (Huo et al., 2014). The singularity problem at the turning points (extinction and ignition) is circumvented using an improved two-point flame-controlling continuation method (Nishioka et al., 1996). The flame solution can transit smoothly across these turning points.

Chelliah et al. (1991) showed that the plug-flow boundary condition is more suitable for counterflow burners. It is thus employed at the two opposed inlets in the present study. The distance between the two inlets is fixed to $L = 2$ cm, with the fuel inlet at $x = 0$ and the oxidizer inlet at $x = L$. The flow strain rate is defined as the absolute maximum velocity gradient in the flowfield, which generally occurs in the mixing zone on the fuel side.

RESULTS AND DISCUSSION

Counterflow diffusion flames of oxygen and *n*-alkane hydrocarbon fuels (CH_4-$C_{16}H_{34}$) are investigated systematically. Emphasis is focused on the effects of inlet temperature, pressure, and strain rate on the flame characteristics. As benchmarks, detailed behaviors of oxygen/methane and oxygen/*n*-heptane systems are analyzed at both subcritical and supercritical conditions. A general correlation is then obtained to identify the common features of the *n*-alkane family (CH_4-$C_{16}H_{34}$). Table 1 lists the critical properties of oxygen, hydrogen, and selected *n*-alkane fuels (Linstrom and Mallard, 2014).

Oxygen/Methane System

Table 2 provides the chemical kinetic mechanisms employed in the present study for oxygen and *n*-alkane fuels. The oxygen/methane chemical scheme developed by Petersen et al. (1999) consists of 38 species and 190 reaction steps. It was validated against shock-tube experiments at pressures up to 260 atm, temperatures as low as 1040 K, and equivalence ratios up to 6. The mechanisms for C_2H_6-$C_{16}H_{34}$ were validated with pressures up to 80 atm and temperatures in the range of 650–1600 K.

As a validation procedure, the property evaluation scheme is examined carefully. Figures 2 and 3 show the calculated compressibility factor (Z), density (ρ), specific heat at constant pressure (C_p), and thermal conductivity (λ) for oxygen and methane, respectively. They match closely with the NIST data (Linstrom and Mallard, 2014). The temperature range covers both the subcritical and supercritical regimes. The property anomalies in the

Table 1 Critical properties

Reactants	T_{cr} (K)	p_{cr} (atm)	V_{cr} (cm^3/mol)
O_2	154.6	49.8	73.4
H_2	33.2	12.8	65.0
CH_4	190.6	45.6	98.6
C_7H_{16}	540.0	27.0	428.0
$C_{12}H_{26}$	658.2	17.9	754.0
$C_{16}H_{34}$	722.0	13.8	1034.0

Table 2 Reaction mechanisms of O_2 with H_2 and *n*-alkanes (CH_4-$C_{16}H_{34}$)

Fuels	Number of species	Number of reactions	Reference
H_2	9	21	Ó Conaire et al. (2004)
CH_4	38	190	Petersen et al. (1999)
C_2H_6	155	689	Marinov et al. (1998)
C_3H_8	155	689	Marinov et al. (1998)
C_4H_{10}	155	689	Marinov et al. (1998)
C_5H_{12}	560	2538	Curran et al. (1998)
C_6H_{14}	560	2538	Curran et al. (1998)
C_7H_{16}	560	2538	Curran et al. (1998)
C_8H_{18}	691	2992	Westbrook et al. (2009)
$C_{10}H_{22}$	952	3899	Westbrook et al. (2009)
$C_{12}H_{26}$	1078	5056	Westbrook et al. (2009)
$C_{14}H_{30}$	1666	6476	Westbrook et al. (2009)
$C_{16}H_{34}$	2115	8157	Westbrook et al. (2009)

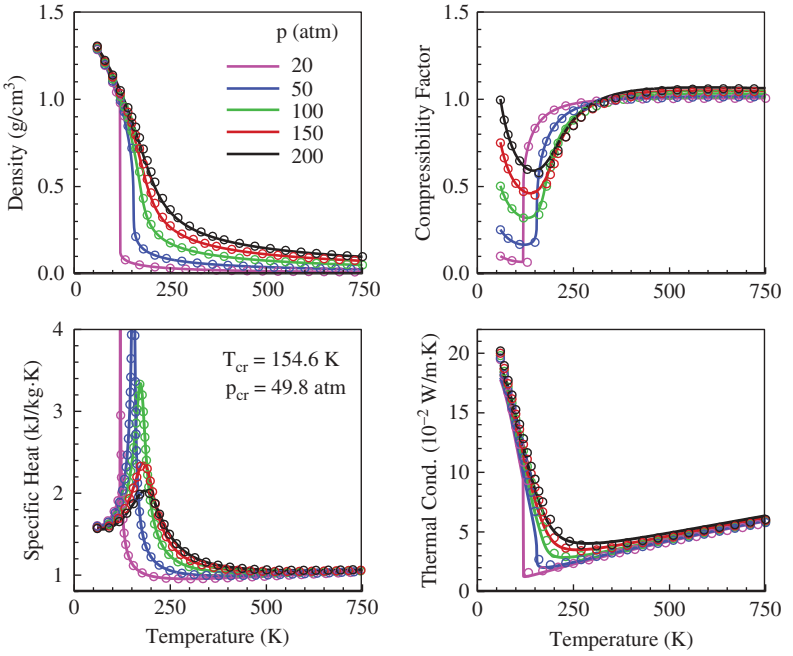

Figure 2 Thermodynamic and transport properties of oxygen validated against NIST data. Lines: the present scheme; symbols: NIST data.

vicinity of the critical point (Yang, 2000) are clearly observed. The abrupt variations at the subcritical pressure (20 atm) arise from the phase change from dense liquid to light gas. This phenomenon disappears, however, at supercritical pressures, rendering smooth and continuous transitions with the temperature.

Figure 4 shows the distributions of thermophysical properties in the flame zone with oxygen and methane inlet temperatures of 120 K and 300 K, respectively. The pressure is 100 atm and the flow strain rate is 90 s^{-1}. The compressibility factor varies rapidly from

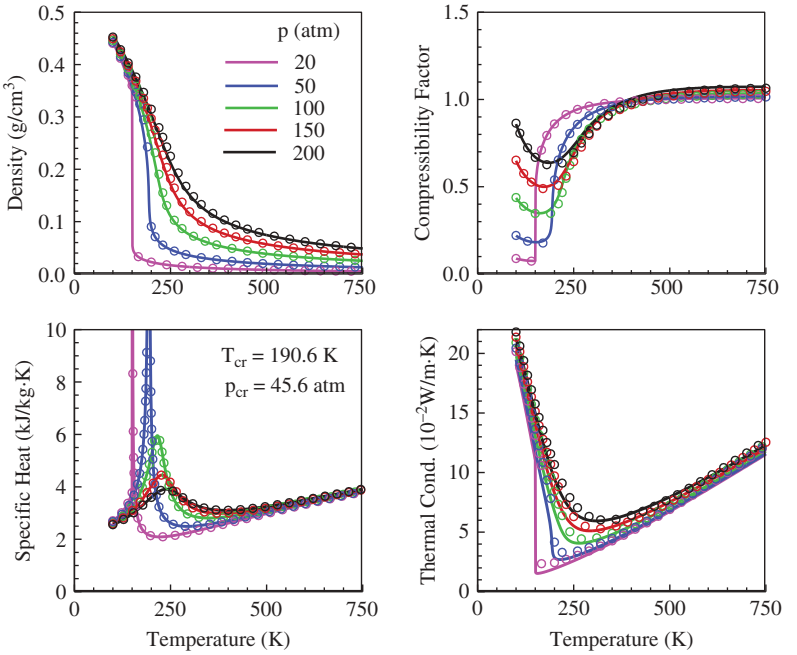

Figure 3 Thermodynamic and transport properties of methane validated against NIST data. Lines: the present scheme; symbols: NIST data.

0.3 to 1.0 in a thin region on the oxygen side when the local temperature increases across the critical point of 154.6 K. The corresponding density drops sharply from 1.0 to 10^{-4} g/cm^3. Similar phenomena occur for other thermodynamic and transport properties. In spite of such steep changes of fluid properties in the low-temperature region on the oxygen side, the oxygen stream heats up rapidly and behaves like a perfect gas before entering the flame zone.

Figure 5 shows the flame structures at 100 atm with three different oxygen inlet temperatures of 120 K, 300 K, and 500 K, covering both the subcritical and supercritical regimes. The methane inlet temperature remains fixed at 300 K and the strain rate is $a = 1000\ \text{s}^{-1}$. In spite of the distinct distributions of flow properties with different oxygen inlet temperatures in the physical space, the property distributions in the mixture-fraction space collapse into single profiles, especially in the flame zone. The case with $T_{O_2} = 500$ K features a slightly wider flame. The distribution of heat-release rate exhibits two peaks and one valley. The latter is caused by dominant effects of pyrolysis-type reactions that occur endothermically on the fuel side. Figure 6 shows the effect of the oxygen inlet temperature on the flame extinction at two different pressures. The extinction strain rate moderately increases almost linearly with increasing T_{O_2}, whereas the maximum flame temperature at extinction remains nearly constant. Overall, the oxygen inlet temperature has a negligible effect on the flame structure, as can be predicted using an ideal-gas assumption. If the inlet temperature falls in the cryogenic fluid range (e.g., $T_{O_2} = 120$ K), real-fluid effects must be taken into account to accurately capture the local flow development.

Figure 7 shows the distributions of the temperature and mass fractions of oxygen and methane throughout the flowfield at pressures of 1–150 atm. The inlet temperature is set

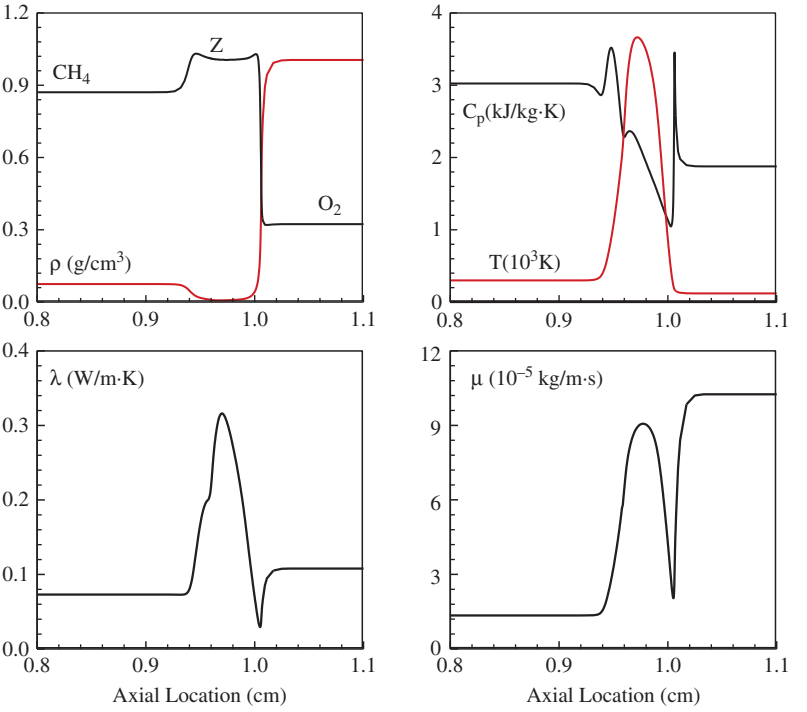

Figure 4 Distributions of thermophysical properties in the axial direction. Oxygen/methane system with $p = 100$ atm, $T_{O_2} = 120$ K, $T_{CH_4} = 300$ K, and $a = 90$ s^{-1}.

to 300 K for both reactants, and the flow strain rate is fixed at 1000 s^{-1}. The peak flame temperature increases progressively with pressure, while the flame thickness decreases significantly with increasing pressure. Methane and oxygen are consumed completely in the flame region, a situation referred to as intensively stable burning. Because of the variation of the flame thickness with pressure, the temperature and species fields exhibit distinct profiles in the physical space.

The situation in the mixture-fraction space shown in Figure 8, however, becomes fundamentally different with all the data collapsed to a single distribution, regardless of the pressure. Seshadri and Peters (1988) divided a methane-air diffusion flame into three distinct zones: the fuel-consumption zone, the water-gas shift, and the H_2-CO oxidation zones. In the present study, the fuel-consumption zone on the methane side is clearly displayed in Figure 8a. The mass fractions of H_2 and CO reach their maxima where the methane concentration diminishes. The H_2-CO oxidation layer is located on the oxygen side, where the maxima of H_2O and CO_2 concentrations occur. The mass fractions of the intermediate species shown in Figure 8c reveal different behaviors with respect to pressure. While the O and H concentrations decrease with increasing pressure as radical recombination reactions are strengthened, the OH concentration does not indicate such a monotonic trend, because of the competition of chain-branching and radical-recombination reactions at high pressure. As a result, in the mixture fraction space, the major species exhibit similar behaviors, while those of the intermediate species are distinctly distributed with pressure. The latter play a crucial role in determining heat-release properties through radical reactions.

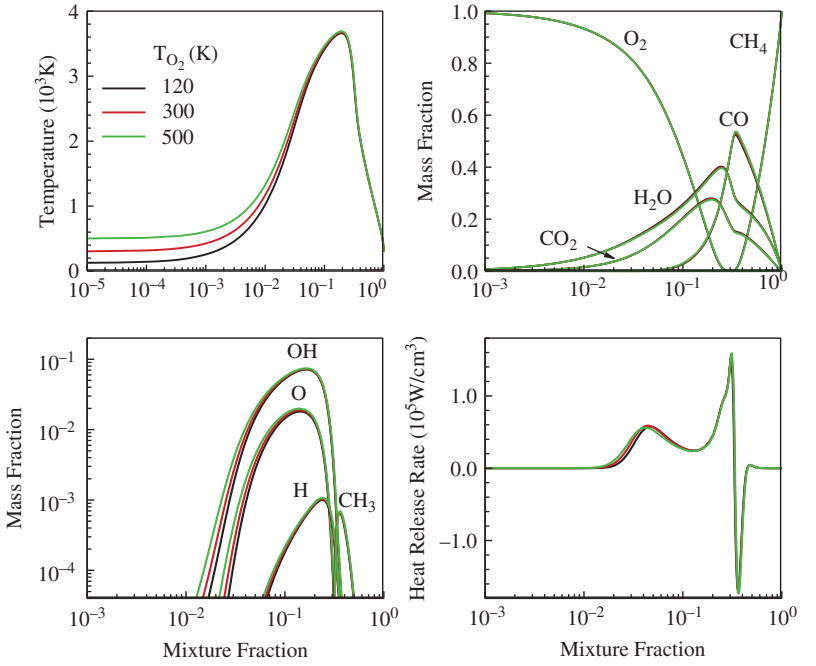

Figure 5 Distributions of temperature, species mass fractions, and heat-release rate in the mixture fraction space. Oxygen/methane system with $p = 100$ atm, $T_{CH_4} = 300$ K, and $a = 1000$ s^{-1}.

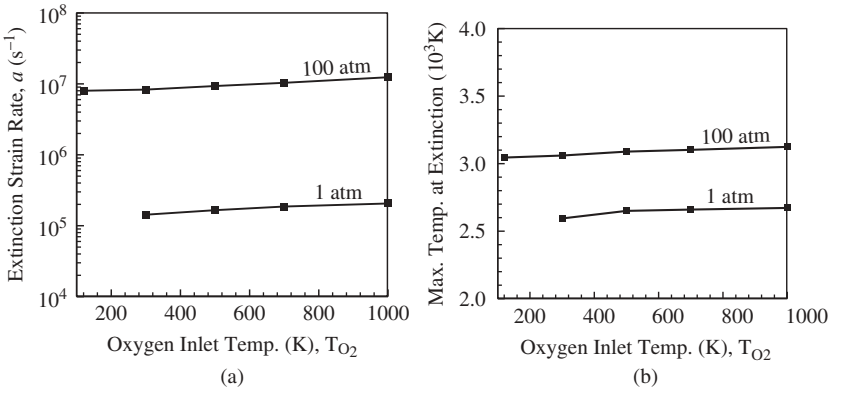

Figure 6 Effects of oxygen inlet temperatures on extinction properties: (a) strain rate; (b) maximum flame temperature. Oxygen/methane system with $T_{CH_4} = 300$ K.

Figure 9 shows the maximum flame temperature as a function of strain rate at various pressures. The inlet temperatures for both methane and oxygen are fixed at 300 K, and the momentum fluxes at the two boundaries are set to be equal in order to place the stagnation plane at the center for all cases. The stable (upper) and unstable (middle) burning branches of the S-curve are obtained. The weakly reacting (lower) branch is not present here because the inlet temperature of 300 K is well below the ignition point.

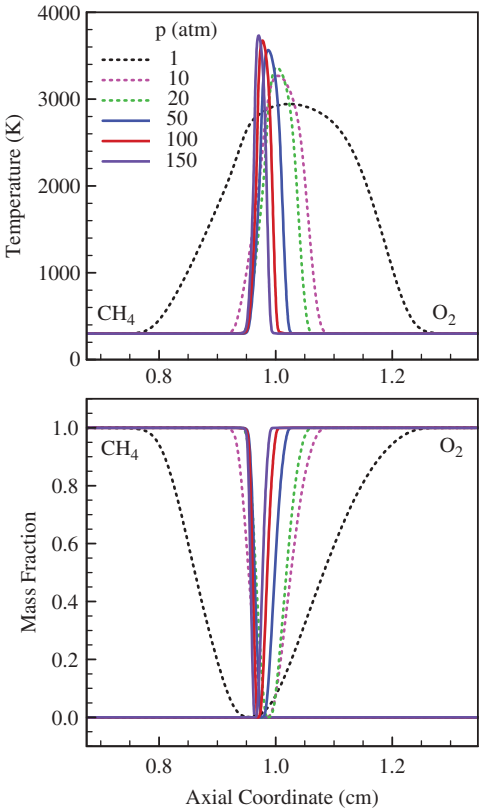

Figure 7 Distributions of temperature and mass fractions of methane and oxygen at different pressures. Oxygen/methane system with $T_{O_2} = T_{CH_4} = 300$ K and $a = 1000\ s^{-1}$.

The flame behaviors bear close similarity to those of the oxygen/hydrogen system discussed in Huo et al. (2014), in which detailed physical explanations are provided. For a given strain rate, the maximum flame temperature increases with pressure as a result of the reduced dissociation associated with endothermic reactions. The maximum flame temperature remains almost constant at low strain rates, and starts to decrease progressively until the extinction point is reached. At low strain rates, the chemical time scale is much smaller than the flow time scale. Thermal energy released by chemical reactions overrides heat loss. A further increase in the strain rate, however, renders the flow time scale comparable to its chemical counterpart. The ensuing heat loss leads to a lower flame temperature and eventually to flame extinction.

Figure 10 shows the effects of pressure on the peak flame temperature and flow strain rate at the extinction point. The extinction strain rate is almost linearly proportional to pressure, up to 50 atm. Its rate of increase then drops slightly after this point. At low pressures ($p < 50$ atm), the extinction is dominated by second-order chain-branching reactions. The chemical time scale is inversely proportional to pressure; a linear relationship thus exists between the extinction strain rate and pressure (Sohn et al., 1998). At high pressures ($p > 50$ atm), the crossover temperature characterizing radical-recombination reactions increases faster than the peak temperature for chain-branching reactions. Radical-recombination

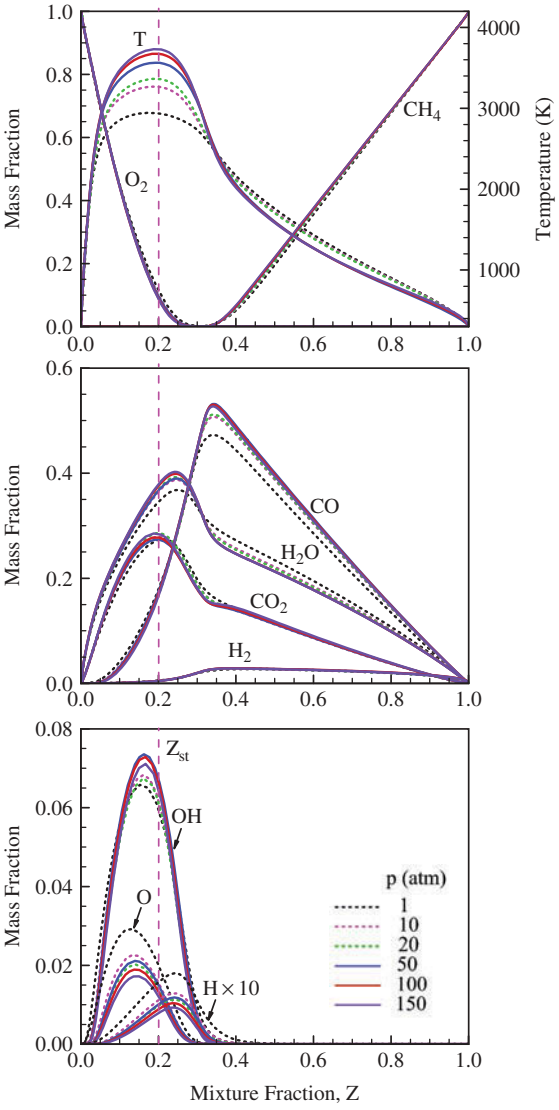

Figure 8 Distributions of temperature and species mass fractions at different pressures in the mixture-fraction space. Oxygen/methane system with $T_{O_2} = T_{CH_4} = 300$ K and $a = 1000\ \text{s}^{-1}$.

reactions consequently play a more influential role and cause the bend-over of the curve. The peak flame temperature at extinction T_{ext} increases with increasing pressure in a manner similar to that for the equilibrium flame temperature T_{eq}, as listed in Table 3. Power-law relationships can be established between the peak flame temperature and pressure: $T_{eq} \sim p^{0.0474}$ in equilibrium, $T_{ext} \sim p^{0.0383}$ at extinction. This information will be employed in the scaling analysis of the heat-release rate. Figure 11 shows the flame response along the S-curve for the oxygen/hydrogen and oxygen/methane systems at 50 atm. The extinction strain rate for hydrogen ($\sim 10^7\ \text{s}^{-1}$) is an order of magnitude larger than that for methane ($\sim 10^6\ \text{s}^{-1}$). The oxygen/hydrogen flame is significantly more resistant to the flow straining

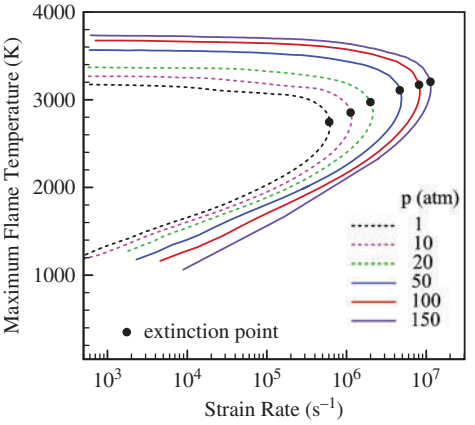

Figure 9 Effects of flow strain rate on maximum flame temperature at different pressures. Oxygen/methane system with $T_{O_2} = T_{CH_4} = 300$ K.

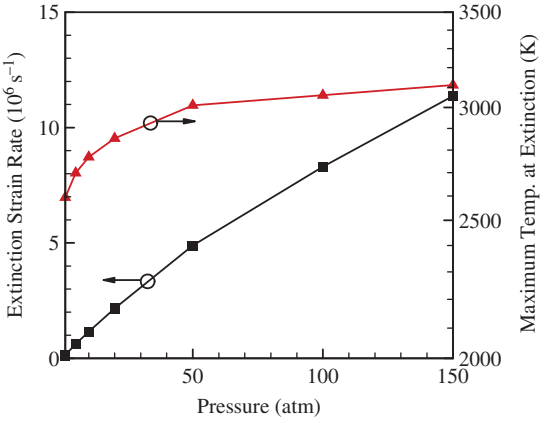

Figure 10 Effects of pressure on strain rate and maximum temperature at extinction. Oxygen/methane system with $T_{O_2} = T_{CH_4} = 300$ K.

Table 3 Maximum flame temperature at equilibrium and extinction state for the oxygen/methane system

Pressure (atm)	1	5	10	20	50	100	150
T_{eq} (K)	2953	3174	3268	3370	3566	3650	3741
T_{ext} (K)	2594	2699	2769	2854	3011	3060	3111

than its oxygen/methane counterpart. This may be attributed to the greater thermal and mass diffusivities and faster kinetics of hydrogen.

In order to extract more information about extinction characteristics at different pressures, the distributions of temperature and species concentrations at the extinction point are plotted in the mixture-fraction space, as shown in Figure 12. The inlet temperatures are $T_{CH_4} = T_{O_2} = 300$ K. The extinction flame temperature increases with increasing pressure. Figure 12a indicates that unburned oxygen penetrates into the methane stream at extinction,

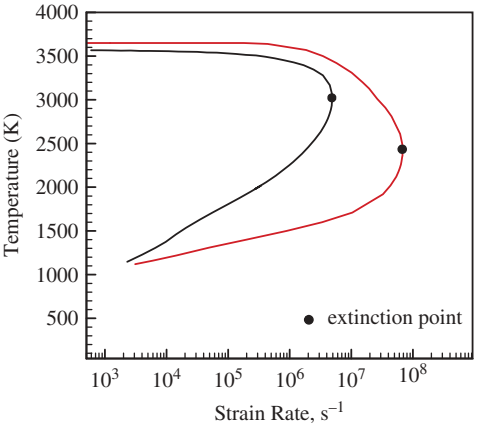

Figure 11 Flame response along the S-curve for oxygen/hydrogen and oxygen/methane systems at $p = 50$ atm with $T_{O_2} = T_{H_2} = T_{CH_4} = 300$ K.

and the methane reacts completely in the flame zone. The oxygen penetration declines at higher pressures, which explains the increase in peak temperature with increasing pressure. Figures 12b and 12c present the mass-fraction distributions of major and minor species at extinction. The production of H_2O and CO_2 increases with pressure, whereas production of other species, such as CO, O, OH, and H, decreases. High flame temperature tends to facilitate the decomposition of oxygen, which outweighs the reduction of oxygen dissociation at high pressure and consequently results in decreased presence of oxygen across the flame. The H_2-CO oxidation is intensified at high pressure, leading to increased H_2O and CO_2 concentrations and lower concentrations of other species, as evidenced in Figures 12b and 12c.

Figure 13a shows the global heat-release rate $\dot{q}$ as a function of the strain rate over a pressure range of 1–150 atm. The result is obtained by integrating the local heat-release rate over the entire flame zone. In the stable-burning (upper) branch of the S-curve at a given pressure, the heat-release rate increases linearly with the strain rate because of the increased mass flow rate. It reaches a maximum and then decreases toward the extinction point. The behaviors near the extinction point are well captured. The heat-release rate in the unstable-burning (lower) branch is also obtained for the first time for the oxygen/methane system using a real-fluid approach. The results in Figure 13b confirm the previous finding of Pons et al. (2008) that $\dot{q} \sim \sqrt{pa}$ in the stable-burning branch except for the region in the vicinity of the extinction point. A similar trend for the oxygen/hydrogen system was observed by Ribert et al. (2008) and Huo et al. (2014).

To identify intrinsic flame similarities at different pressures, a scaled heat-release rate, defined by $\hat{\dot{q}} = \dot{q}/\sqrt{pa_{ext}}$, is plotted as a function of a normalized strain rate, a/a_{ext}, as shown in Figure 14a. The profiles very nearly collapse to a single curve. Huo et al. (2014) developed a scaling analysis and found that to obtain a more accurate result, an additional pressure exponent accounting for the effect of pressure on the peak flame temperature should be included:

$$\dot{q} \sim \frac{\bar{T}_{eq}^{0.75}}{MW_{mix}^{0.25}}\sqrt{pa} \tag{1}$$

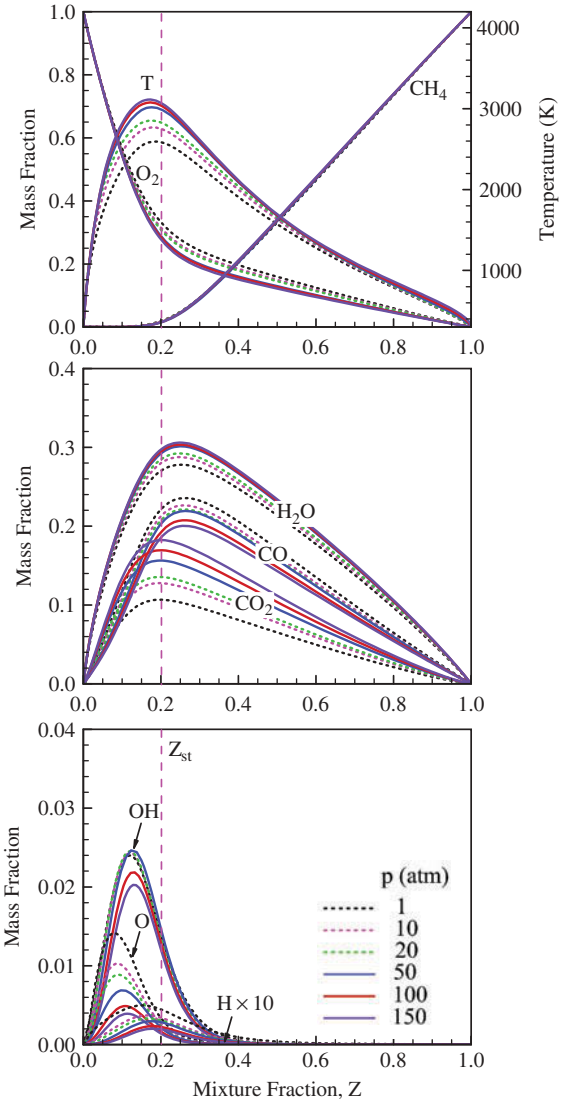

Figure 12 Distributions of temperature and species mass fractions at the extinction point in the pressure range of 1–150 atm. Oxygen/methane system with $T_{O_2} = T_{CH_4} = 300$ K.

Substitution of the pressure dependence of the flame temperature, $\bar{T}_{eq} \sim p^{0.0474}$, into the above equation gives the following correlation for the heat-release rate:

$$\dot{q} \sim p^{0.536}\sqrt{a} \tag{2}$$

Figure 14b shows this new scaled heat-release rate:

$$\hat{\dot{q}} = \dot{q}/p^{0.536}\sqrt{a_{ext}} \tag{3}$$

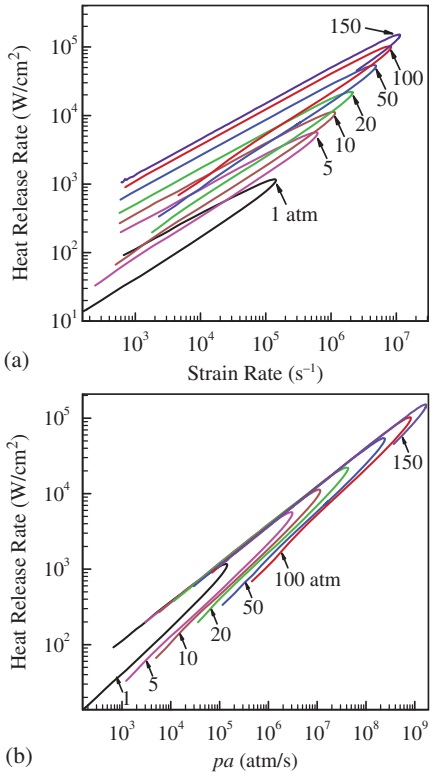

Figure 13 Distributions of global heat-release rate as a function of strain rate in the pressure range of 1–150 atm. Oxygen/methane system with $T_{O_2} = T_{CH_4} = 300$ K.

which allows for the collapse of all the heat-release rate profiles to a single function of the normalized strain rate, a/a_{ext}. This flame similarity implies that the heat-release behaviors at high pressure can be obtained from their counterparts at low pressure through proper scaling analysis.

Like the heat-release rate, the flame thickness δ, defined as the full width at half maximum of the temperature distribution, correlates well with the product of pressure and flow strain rate, pa, as shown in Figure 15. In the stable burning (upper) branch (except in the vicinity of the extinction point), the flame thickness exhibits the following trend:

$$\delta \sim 1/\sqrt{pa} \tag{4}$$

The strong flame similarity at various pressures can be further consolidated using a scaled flame thickness, $\hat{\delta} \equiv \delta\sqrt{pa_{ext}}$, and a normalized flow strain rate, a/a_{ext} (Huo et al., 2014). Figure 16 shows the result. Similar correlations exist for major species distributions as elaborated by Huo et al. (2014) for the oxygen/hydrogen system. The flame characteristics at high pressure can be predicted from the corresponding results at low pressure.

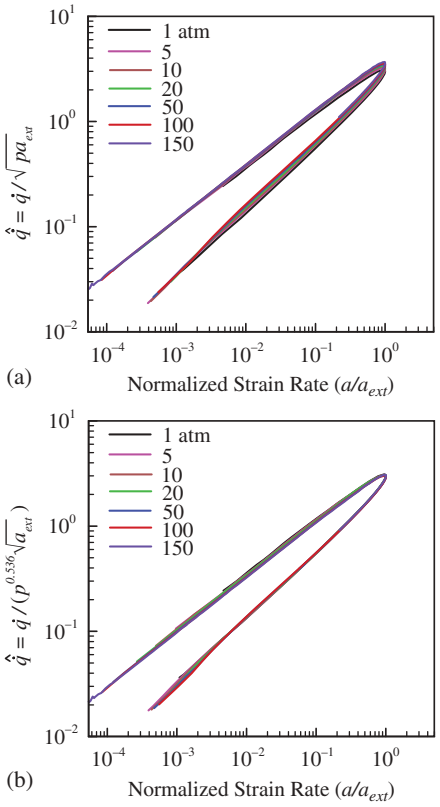

Figure 14 Scaled heat-release rate $\hat{q}$ as a function of normalized strain rate (a/a_{ext}). Oxygen/methane system with $T_{O_2} = T_{CH_4} = 300$ K. (a) $\hat{q} = \dot{q}/\sqrt{pa_{ext}}$; (b) $\hat{q} = \dot{q}/p^{0.536}\sqrt{a_{ext}}$.

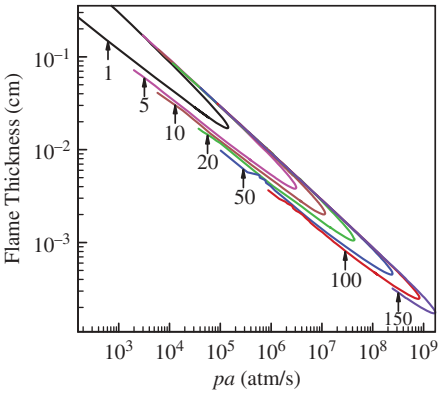

Figure 15 Flame thickness as a function of strain rate in the pressure range of 1–150 atm. Oxygen/methane system with $T_{O_2} = T_{CH_4} = 300$ K.

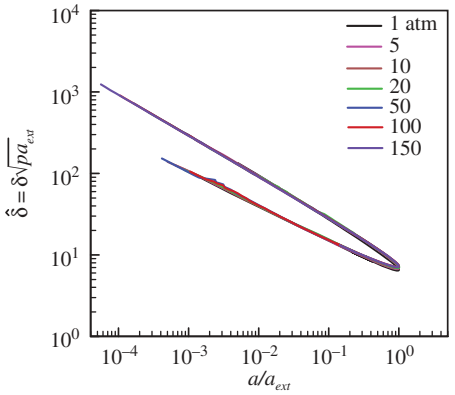

Figure 16 Scaled flame thickness $\hat{\delta} = \delta\sqrt{pa_{ext}}$ as a function of normalized strain rate (a/a_{ext}). Oxygen/methane system with $T_{O_2} = T_{CH_4} = 300$ K.

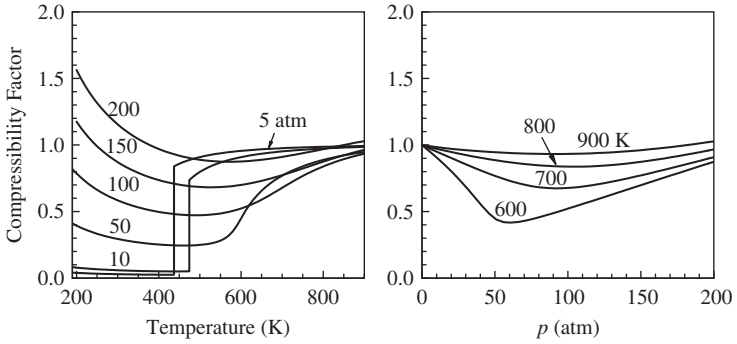

Figure 17 Compressibility factor of *n*-heptane at different pressures and temperatures.

Oxygen/*n*-Heptane System

n-Heptane, C_6H_{14}, is a primary reference fuel for the study of combustion in internal combustion engines, due to its zero octane rating. The detailed chemical mechanism developed by Curran et al. (1998), including 560 species and 2538 reversible reactions, is employed in the present study, as listed in Table 2. This mechanism has been validated against experimental data obtained from flow reactors, shock tubes, and rapid compression machines over the pressure and temperature ranges of 3 atm to 50 atm and 650 K to 1200 K, respectively. To avoid complexities associated with fuel vaporization, the inlet temperature remains at 600 K or above in the present study. Figure 17 shows the variation of the compressibility factor with pressure and temperature. At 600 K, the compressibility factor reaches as small as 0.4 for $p = 60$ atm. It approaches unity when the temperature exceeds 900 K. As noted previously (Huo et al., 2014; Ribert et al., 2008), the real-fluid effect takes place only in the region close to a low-temperature, high-pressure inlet. The fluid essentially behaves like an ideal gas when it approaches the flame zone. In light of this, the real-fluid property evaluations are neglected here for simplicity.

Figure 18 shows the distributions of the temperature and mass fractions of major species. *n*-Heptane first decomposes to intermediate species of C_2H_2 and C_2H_4, and then

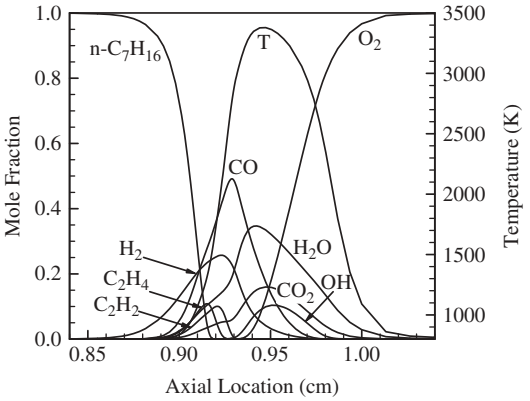

Figure 18 Distributions of temperature and mass fractions of major species. Oxygen/*n*-heptane system with $p = 10$ atm, $T_{O_2} = T_{C_7H_{16}} = 800$ K, and $a = 1000\ \text{s}^{-1}$.

produces H_2 and CO on the fuel side. The maximum of H_2O and CO_2 mole fractions occurs close to the oxygen side. Figure 19 shows the effects of the inlet temperature on the flame properties, including the maximum flame temperature, flame thickness, and heat-release rate, at various pressures. The flow strain rate remains fixed at 1000 s^{-1}. As in the oxygen/methane system, the disparities of flame properties for different inlet temperatures appear to be quite modest at a given pressure, indicating the negligible influence of the inlet temperature on the flame response.

Figure 20 shows the variations of the heat-release rate and flame thickness as a function of strain rate over the pressure range of 1–200 atm. Only the results for the stable burning branch of the S-curve are presented. The flame behaviors near the extinction point and in the unstable burning branch can be captured following the same approach for the oxygen/methane system. The heat-release rate increases linearly with the strain rate, and the flame thickness decreases in a linear manner. As in the oxygen/methane system, the heat-release rate and flame thickness correlates well as $\dot{q} \sim \sqrt{pa}$ and $\delta \sim 1/\sqrt{pa}$. The former correlation can be further modified to account for the pressure dependence of the peak flame temperature, as described in the previous section. Substitution of the flame temperature-pressure relation obtained from Figure 19a, $\bar{T}_{eq} \sim p^{0.045}$, into Eq. (1) gives the following correlation of the heat-release rate for the oxygen/*n*-heptane system:

$$\dot{q} \sim p^{0.534}\sqrt{a} \tag{5}$$

The pressure exponent of 0.534 coincides with that of the oxygen/hydrogen system (Huo et al., 2014). An identical scaling can thus be achieved for the flame thickness and heat-release rate using Eqs. (4) and (5), respectively, in the normalized strain rate space. The intrinsic similarities of the flame response are obtained for the oxygen/*n*-heptane system in a broad range of pressures and strain rates.

Oxygen/*n*-Alkane (CH_4-$C_{16}H_{34}$) Systems

The common features of oxygen/methane and oxygen/*n*-heptane flames suggest that the same kind of flame similarities may be applied to the entire *n*-alkane family

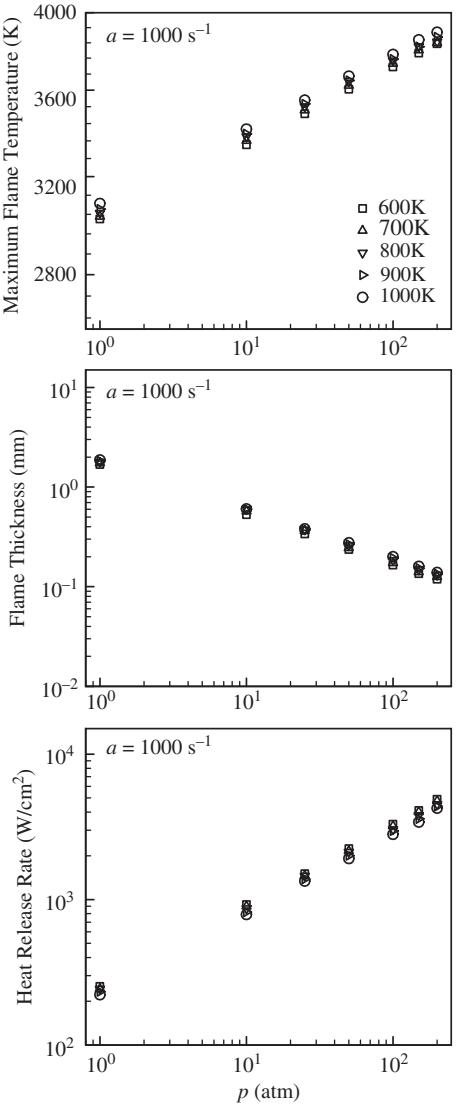

Figure 19 Effects of inlet temperature on (a) flame maximum temperature, (b) flame thickness, and (c) heat-release rate at different pressures for oxygen/*n*-heptane system.

(CH_4-$C_{16}H_{34}$). Table 2 lists the detailed chemical mechanisms of the *n*-alkanes employed in the present study. Figure 21 shows the compressibility factors for *n*-dodecane ($C_{12}H_{26}$) and *n*-hexadecane ($C_{16}H_{34}$) in the pressure-temperature space. The compressibility factor approaches unity when the temperature exceeds 800 K and the pressure is smaller than 100 atm. For simplicity, all of the calculations are conducted at this inlet temperature, with the ideal-gas equation of state implemented for property evaluations. Figure 22 shows the flame properties as a function of the number of carbons in the *n*-alkane fuel molecule. Also included is pure hydrogen. The strain rate is set to 1000 s^{-1} and the pressure to 10 atm. Hydrogen has a much higher maximum flame temperature and a wider flame zone, as well

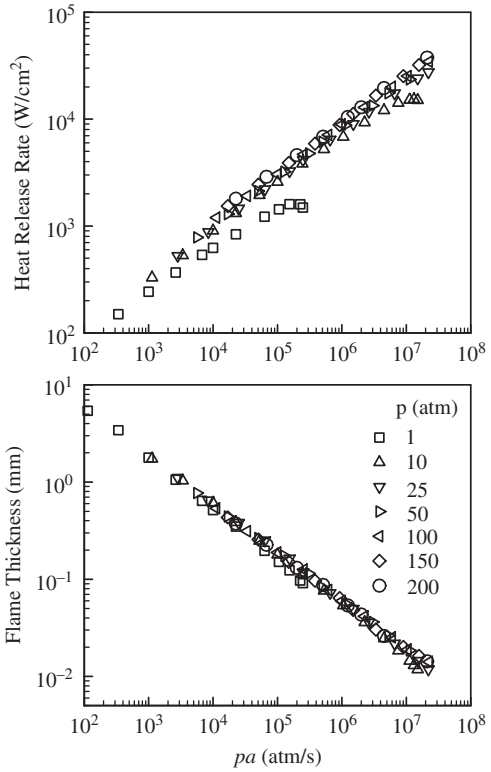

Figure 20 Distributions of the heat-release rate and flame thickness as a function of strain rate in the pressure range of 1 to 200 atm. Oxygen/*n*-heptane system with $T_{O_2} = T_{C_7H_{16}} = 800$ K.

as greater heat release, than all members in the alkane family. The flame thickness for the *n*-alkanes is nearly the same regardless of the number of carbons. The peak flame temperature increases slightly with increasing number of carbons from 3350 K for CH_4 and levels off at 3800 K when the carbon number exceeds 5. The heat-release rate experiences a sharp increase from methane to ethane, and then decreases gradually to saturate at *n*-pentane. The flame properties of heavy hydrocarbons (C_5-C_{16}) are nearly identical. Light hydrocarbons exhibit distinct flame behaviors, mainly due to the variation of the carbon-hydrogen mass ratio, which changes significantly when the number of carbons varies from 0 to 5. Although not shown here, the flame thickness and heat-release rate of all hydrocarbon fuels can be correlated with pressure and strain rate in a manner similar to those of methane and *n*-heptane. The flame properties at high pressure can be obtained from their counterpart at low pressure.

Figure 23 shows the scaled flame thickness ($C = \delta\sqrt{pa}$) as a function of the number of carbons in the *n*-alkane fuel molecule. The scaled flame thickness remains nearly constant for all hydrocarbons at the given pressure and strain rate. The flame properties of a given hydrocarbon fuel can be evaluated by those of another hydrocarbon fuel at the same flow conditions. The validity of scaling and similarity becomes even greater if the carbon numbers of the two hydrocarbons of concern are higher than 5. This finding can be effectively used to considerably improve computational efficiency for the modeling of oxygen/hydrocarbon turbulent flames using tabulated chemistry.

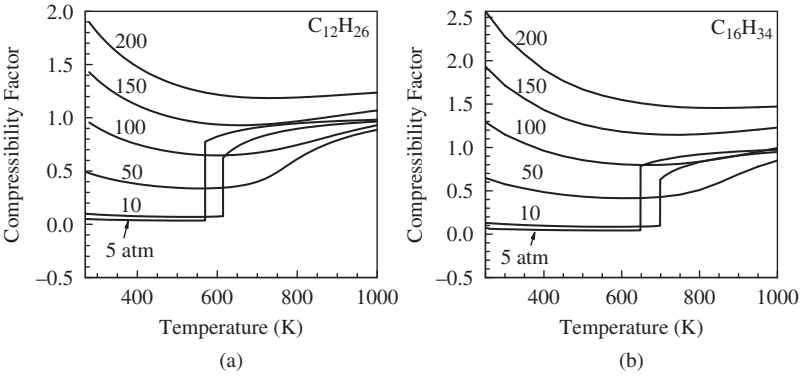

Figure 21 Compressibility factors of (a) $C_{12}H_{26}$ and (b) $C_{16}H_{34}$ at different pressures and temperatures.

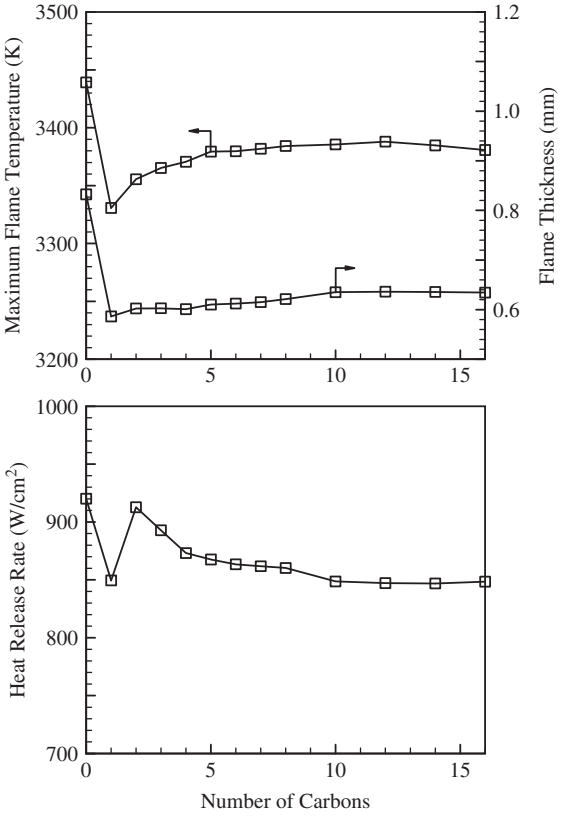

Figure 22 Maximum flame temperature, flame thickness, and heat-release rate as a function of number of carbons in the *n*-alkane fuel molecule. Oxygen/hydrogen and oxygen/*n*-alkanes systems with $p = 10$ atm, $T_{O_2} = T_{Fuel} =$ 800 K, and $a = 1000\ \text{s}^{-1}$.

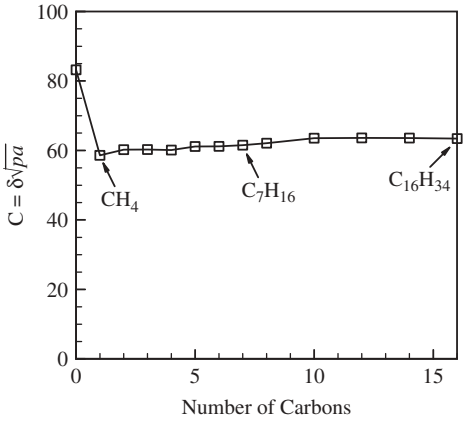

Figure 23 Flame thickness parameter ($C = \delta\sqrt{pa}$) as a function of number of carbons in the *n*-alkane fuel molecule. Oxygen/hydrogen and oxygen/*n*-alkanes systems with $p = 10$ atm, $T_{O_2} = T_{Fuel} = 800$ K, and $a = 1000\ s^{-1}$.

CONCLUSION

A systematic investigation of counterflow diffusion flames of oxygen and *n*-alkanes (CH_4-$C_{16}H_{34}$) has been conducted. The numerical framework incorporates fundamental thermodynamics and transport theories for general fluids, detailed chemical mechanisms, and an improved flame-controlling continuation method. The flame response over the entire S-curve is explored under a broad range of pressures, flow strain rates, and inlet temperatures. The main conclusions are as follows:

1. The inlet temperature yields insignificant effects on the flame structure; ideal gas flame solutions can be used for fluids at supercritical conditions.
2. For the oxygen/methane system, the flow strain rate at the extinction point increases linearly with pressure up to 50 atm, but the rate of increase decreases beyond this point. The extinction characteristics for other *n*-alkanes follow a similar trend.
3. The flame thickness of all hydrocarbon fuels is inversely proportional to the square root of the product of pressure and strain rate, $\delta \sim \sqrt{pa}$, and all profiles of scaled flame thickness collapse to a single curve in the normalized strain-rate space (a/a_{ext}). At a given pressure and strain rate, the scaled flame thickness ($C = \delta\sqrt{pa}$) of all hydrocarbon fuels has nearly an identical value.
4. The global heat-release rate is proportional to the square root of the pressure-weighted strain rate, $\dot{q} \sim \sqrt{pa}$, or more precisely proportional to $p^{0.536}\sqrt{a}$ for methane and to $p^{0.534}\sqrt{a}$ for *n*-heptane, when the pressure effect on the peak flame temperature is taken into account. With this correlation, the profiles of the scaled heat-release rate for all pressures under consideration overlap completely as a function of the normalized strain rate, a/a_{ext}.

The similarities of flame properties among the *n*-alkane family suggest that the flame solutions of any *n*-alkane at a given pressure can be predicted from those of another *n*-alkane at another pressure provided that the value of pa is the same. This will significantly

improve the computational efficiency of turbulent combustion modeling using tabulated chemistry.

ACKNOWLEDGMENT

The authors gratefully acknowledge the support and advice given by Dr. Mitat A. Birkan.

FUNDING

This work was sponsored by the Air Force Office of Scientific Research under Grant No. FA 9550-10-1-0179.

NOMENCLATURE

a	flow strain rate
a_{ext}	extinction strain rate
C_p	specific heat at constant pressure
L	distance of two inlets
MW_{mix}	molecular weight of mixture
p	pressure
$\dot{q}$	global heat-release rate
$\hat{\dot{q}}$	scaled heat-release rate
T_{ext}	maximum flame temperature at extinction
T_{eq}	maximum flame temperature at equilibrium
T_{O_2}	oxygen inlet temperature
T_{CH_4}	methane inlet temperature
V	molar specific volume
x	axial coordinate
Z	compressibility factor
Z_{st}	stoichiometric mixture fraction

Greek Symbols

ρ	density of mixture
λ	thermal conductivity
μ	dynamic viscosity
δ	flame thickness
$\hat{\delta}$	scaled flame thickness

Subscripts

cr	thermodynamic critical state
mix	mixture
eq	equilibrium
ext	extinction

REFERENCES

Chelliah, H., Law, C., Ueda, T., Smooke, M., and Williams, F. 1991. An experimental and theoretical investigation of the dilution, pressure and flow-field effects on the extinction condition of methane-air-nitrogen diffusion flames. *Proc. Combust. Inst*., **23**, 503.

Curran, H., Gaffuri, P., Pitz, W.J., and Westbrook, C.K. 1998. A comprehensive modeling study of n-heptane oxidation. *Combust. Flame*, **114**, 149.

Huo, H., Wang, X., and Yang, V. 2014. A general study of counterflow diffusion flames at subcritical and supercritical conditions: Oxygen/hydrogen mixtures. *Combust. Flame*, **161**(12), 3040–3050.

Kee, R.J., Miller, J.A., Evans, G.H., and Dixon-Lewis, G. 1989. A computational model of the structure and extinction of strained, opposed flow, premixed methane-air flames. *Symp. (Int.) Combust*., **22**, 1479.

Lacaze, G., and Oefelein, J.C. 2012. A non-premixed combustion model based on flame structure analysis at supercritical pressures. *Combust. Flame*, **159**, 2087.

Law, C.K. 2006. *Combustion Physics*, Cambridge University Press, Cambridge, UK.

Li, S., and Williams, F. 2000. Counterflow heptane flame structure. *Proc. Combust. Inst*., **28**, 1031.

Linstrom, P.J., and Mallard, W.G. (Eds.). 2014. *NIST Chemistry WebBook, NIST Standard Reference Database Number 69*, National Institute of Standards and Technology, Gaithersburg, MD.

Marinov, N.M., Pitz, W.J., Westbrook, C.K., Vincitore, A.M., Castaldi, M.J., Senkan, S.M., and Melius, C.F. 1998. Aromatic and polycyclic aromatic hydrocarbon formation in a laminar premixed n-butane flame. *Combust. Flame*, **114**, 192.

Nishioka, M., Law, C.K., and Takeno, T. 1996. A flame-controlling continuation method for generating S-curve responses with detailed chemistry. *Combust. Flame*, **104**, 328.

Ó Conaire, M., Curran, H.J., Simmie, J.M., Pitz, W.J., and Westbrook, C.K. 2004. A comprehensive modeling study of hydrogen oxidation. *Int. J. Chem. Kinet*., **36**, 603.

Petersen, E.L., Davidson, D.F., and Hanson, R.K. 1999. Kinetics modeling of shock-induced ignition in low-dilution CH_4/O_2 mixtures at high pressures and intermediate temperatures. *Combust. Flame*, **117**, 272.

Pons, L., Darabiha, N., and Candel, S. 2008. Pressure effects on nonpremixed strained flames. *Combust. Flame*, **152**, 218.

Pons, L., Darabiha, N., Candel, S., Ribert, G., and Yang, V. 2009. Mass transfer and combustion in transcritical non-premixed counterflows. *Combust. Theor. Modell*., **13**, 57.

Ribert, G., Zong, N., Yang, V., Pons, L., Darabiha, N., and Candel, S. 2008. Counterflow diffusion flames of general fluids: Oxygen/hydrogen mixtures. *Combust. Flame*, **154**, 319.

Seiser, R., Pitsch, H., Seshadri, K., Pitz, W. and Gurran, H. 2000. Extinction and autoignition of n-heptane in counterflow configuration. *Proc. Combust. Inst*., **28**, 2029.

Seshadri, K., and Peters, N. 1988. Asymptotic structure and extinction of methane-air diffusion flames. *Combust. Flame*, **73**, 23.

Soave, G. 1972. Equilibrium constants from a modified Redlich-Kwong equation of state. *Chem. Eng. Sci*., **27**, 1197.

Sohn, C.H., Chung, S.H., Lee, S.R., and Kim, J.S. 1998. Structure and acoustic-pressure response of hydrogen-oxygen diffusion flames at high pressure. *Combust. Flame*, **115**, 299.

Westbrook, C.K., Pitz, W.J., Herbinet, O., Curran, H.J., and Silke, E.J. 2009. A comprehensive detailed chemical kinetic reaction mechanism for combustion of n-alkane hydrocarbons from n-octane to n-hexadecane. *Combust. Flame*, **156**, 181.

Williams, F.A. 1985. *Combustion Theory*, Addison-Wesley, Reading, MA.

Yang, V. 2000. Modeling of supercritical vaporization, mixing, and combustion processes in liquid-fueled propulsion systems. *Proc. Combust. Inst*., **28**, 925.